

physical issue because they do not lie in the region where the QNMs are a good approximation, it can cause numerical challenges. In Paper I, we deal with the divergence by using the complex plane approach. Here, we adopt an alternative method — hyperboloidal time slicing — which avoids the problematic regions. This enables direct numerical treatments of the reduced second-order Teukolsky equation [35, 36]

$$\mathcal{T}[\Psi_4^{(2)}] = S_4^{(2)}. \quad (2)$$

Using the hyperboloidal slicing, it has been shown that QNMs are eigenvectors of the non-normal time evolution operator [43]. The separability of the Teukolsky equation can be used to find the eigenvectors in a more efficient way, as shown in [44].

Our numerical implementation uses the pseudo-spectral method, where all quantities are expanded in Chebyshev polynomials radially and spin-weighted spherical harmonics in the angular directions. Multiplications are performed using fast transforms from the spectral basis to a grid. All results in this paper have radial expansion truncated at degree $n_{\max} = 63$, the spherical harmonic expansion truncating at $\ell_{\max} = 31$ and with 256 bit floating point numbers from the `MultiFloats` library [45].

To obtain the source term $S_4^{(2)}$, we take a different approach from the analytic treatment used in Paper I— here, the source is computed numerically from the Einstein Tensor. To be specific, we first consider the second-order perturbation of the metric

$$g_{ab} = g_{ab}^{\circ} + \epsilon h_{ab}^{(1)} + \epsilon^2 h_{ab}^{(2)} + \mathcal{O}(\epsilon^3), \quad (3)$$

where ϵ is a book-keeping parameter that counts the orders. The Einstein Tensor, as a functional of the metric, can then be expanded as

$$G_{ab}[g_{ab}] = \epsilon G_{ab}^{(1)}[h_{ab}^{(1)}] + \epsilon^2 G_{ab}^{(2)}[h_{ab}^{(2)}] + \epsilon^2 G_{ab}^{(2)}[h_{ab}^{(1)}, h_{ab}^{(1)}] + \mathcal{O}(\epsilon^3), \quad (4)$$

where $G_{ab}^{(1)}$ and $2G_{ab}^{(2)}$ are the first and second functional derivatives of the Einstein Tensor with respect to the metric. To first order, we take $h_{ab}^{(1)}$ to be a sum of QNMs. We solve for $h_{ab}^{(1)}$ by numerically computing the Hertz potential for QNMs in the Outgoing Radiation Gauge (ORG), using the separation technique described in [44]. Note that for a QNM with frequency ω , $h_{ab}^{(1)}$ will have both frequencies ω and $-\bar{\omega}$, which comes from the complex conjugations necessary to make $h_{ab}^{(1)}$ real.

Next, by imposing Einstein's equations at second order, we get the equation

$$G_{ab}^{(1)}[h_{ab}^{(2)}] = -G_{ab}^{(2)}[h_{ab}^{(1)}, h_{ab}^{(1)}], \quad (5)$$

thus $h_{ab}^{(2)}$ satisfies the linearized Einstein equations with $-G_{ab}^{(2)}[h_{ab}^{(1)}, h_{ab}^{(1)}]/8\pi$ acting as the effective stress-energy

tensor at this order. After computing $G_{ab}^{(2)}[h_{ab}^{(1)}, h_{ab}^{(1)}]$ from the linearized metric $h_{ab}^{(1)}$, we convert it to the source $S_4^{(2)}$ for $\Psi_4^{(2)}[h_{ab}^{(2)}]$ in Eq. (2). Note that while Eq. (5) only provides the source for the part of Ψ_4 that depends linearly on $h_{ab}^{(2)}$, in ORG quadratic contribution to Ψ_4 from $h_{ab}^{(1)}$ vanishes.

Finally, we numerically solve the Teukolsky equations with no-incoming boundary conditions to obtain $\Psi_4^{(2)}$ and $\Psi_0^{(2)}$ for the quadratic modes. More details can be found in the Supplementary Material.

CLASSIFICATION OF MODE COUPLINGS

Quadratic coupling channels can be viewed in two ways. The first perspective traces the relationship from linear parent modes to quadratic daughter modes. Consider two linear QNMs (ℓ_1, m_1, n_1, p_1) and (ℓ_2, m_2, n_2, p_2) , and amplitudes A_1 and A_2 . As discussed above, the linearized metric $h_{ab}^{(1)}$ has four frequency components $\omega_{\ell_1 m_1 n_1}^{p_1}$, $-\bar{\omega}_{\ell_1 m_1 n_1}^{p_1}$, $\omega_{\ell_2 m_2 n_2}^{p_2}$, and $-\bar{\omega}_{\ell_2 m_2 n_2}^{p_2}$, with the amplitudes A_1 , \bar{A}_1 , A_2 and \bar{A}_2 . Consequently, the source term in Eq. (5) yields four quadratic frequencies:

$$\begin{aligned} \omega_{\ell_1 m_1 n_1}^{p_1} + \omega_{\ell_2 m_2 n_2}^{p_2}, & \quad \omega_{\ell_1 m_1 n_1}^{p_1} - \bar{\omega}_{\ell_2 m_2 n_2}^{p_2}, \\ -\bar{\omega}_{\ell_1 m_1 n_1}^{p_1} + \omega_{\ell_2 m_2 n_2}^{p_2}, & \quad -\bar{\omega}_{\ell_1 m_1 n_1}^{p_1} - \bar{\omega}_{\ell_2 m_2 n_2}^{p_2}, \end{aligned}$$

with source terms proportional to the products $A_1 A_2$, $A_1 \bar{A}_2$, $\bar{A}_1 A_2$ and $\bar{A}_1 \bar{A}_2$, respectively. This gives rise to *four* distinct channels through which a pair of linear QNMs can generate QQNMs at different frequencies.

The first perspective, which maps two parent modes to four daughter modes, is often conceptually inconvenient. Instead, it is more intuitive to adopt the opposite viewpoint: *given a QQNM with a certain frequency, what are its parent modes?* To formalize this, we will use the following notation to denote a QQNM:

$$\begin{pmatrix} \ell_1, & m_1, & n_1, & p_1 \\ \ell_2, & m_2, & n_2, & p_2 \end{pmatrix}. \quad (6)$$

Its time and azimuthal dependence is expressed as:

$$\sim e^{-i(\omega_{\ell_1, m_1, n_1}^{p_1} + \omega_{\ell_2, m_2, n_2}^{p_2})t} e^{i(m_1 + m_2)\phi}. \quad (7)$$

With this notation, several key observations can be made. First, the QQNM appears only in the $(m_1 + m_2)$ GW harmonics due to the azimuthal angular selection rule. Second, the notation exhausts all possible QQNMs. Third, different pairs of modes (up to exchange symmetry $1 \leftrightarrow 2$) generally produce distinct frequencies. An exception occurs for Schwarzschild BHs, where spherical symmetry makes QNM frequencies independent of m . Nonetheless, different (m_1, m_2) pairs indicate distinct coupling channels. The total QQNM amplitude in a GW harmonic is the sum of all possible pairs (m_1, m_2) with $m_1 + m_2$ fixed.

The QQNM in Eq. (6) is generated by four linear QNMs:

$$\begin{aligned} (\ell_1, m_1, n_1, p_1), & \quad (\ell_1, -m_1, n_1, -p_1), \\ (\ell_2, m_2, n_2, p_2), & \quad (\ell_2, -m_2, n_2, -p_2), \end{aligned}$$

with respective amplitudes A_1 , A_{-1} , A_2 , and A_{-2} . It is worth noting that while the frequency values of (ℓ_1, m_1, n_1, p_1) and $(\ell_1, -m_1, n_1, -p_1)$ are related via Eq. (1), their amplitudes A_1 and A_{-1} are independent, except in the case of nonprecessing systems, where because of the reflection symmetry we have

$$A_{-1} = (-1)^{\ell_1} \bar{A}_1. \quad (8)$$

The four linear QNMs are coupled through four channels

$$(\ell_1, m_1, n_1, p_1) \otimes (\ell_2, m_2, n_2, p_2), \quad ++, \quad (9a)$$

$$(\ell_1, m_1, n_1, p_1) \otimes (\ell_2, -m_2, n_2, -p_2), \quad +-, \quad (9b)$$

$$(\ell_1, -m_1, n_1, -p_1) \otimes (\ell_2, m_2, n_2, p_2), \quad -+, \quad (9c)$$

$$(\ell_1, -m_1, n_1, -p_1) \otimes (\ell_2, -m_2, n_2, -p_2), \quad --. \quad (9d)$$

Below we will refer to them as $++$, $+-$, $-+$, and $--$, respectively. For example, the $(+-)$ channel corresponds to the interaction where the linear mode $(\ell_2, -m_2, n_2, -p_2)$ generates a frequency component $-\bar{\omega}_{\ell_2 - m_2 n_2}^{-p_2}$ in the linearized metric, which is numerically equal to $\omega_{\ell_2 m_2 n_2}^{p_2}$ due to Eq. (1). This component then interacts with the frequency $\omega_{\ell_1 m_1 n_1}^{p_1}$ generated by the first linear mode (ℓ_1, m_1, n_1, p_1) . Denoting the amplitude of the QQNM as A_Q , we have

$$\begin{aligned} A_Q = & R_{++} A_1 A_2 + R_{+-} A_1 \bar{A}_{-2} + R_{-+} \bar{A}_{-1} A_2 \\ & + R_{--} \bar{A}_{-1} \bar{A}_{-2}. \end{aligned} \quad (10)$$

where the coefficients R 's are fully determined by the dimensionless spin of a Kerr BH. Here we use spin-weighted spherical/spheroidal harmonics as the mode basis to facilitate direct comparison with previous results, such as those from numerical relativity and from Paper I. Alternatively, modes can also be classified by parity, see the Supplementary Material for more details.

For nonprecessing binaries, Eq. (10) reduces to

$$\begin{aligned} R^{\text{total}} \equiv \frac{A_Q}{A_1 A_2} = & R_{++} + (-1)^{\ell_2} R_{+-} \\ & + (-1)^{\ell_1} R_{-+} + (-1)^{\ell_1 + \ell_2} R_{--}, \end{aligned} \quad (11)$$

where we have used Eq. (8). Notice that the right-hand side (RHS) is an intrinsic property of a Kerr BH, independent of the linear mode amplitudes. We define the RHS as the total amplitude ratio R^{total} , which characterizes the excitability of the QQNM.

The $(--)$ channel deserves more attention. We find that R_{--} always vanishes identically, regardless of the types of parent modes and the spin of the Kerr BH. This

result follows directly from the second-order Teukolsky equation in Eq. (2), where the source $S_4^{(2)}$ takes the following form in ORG [18]:

$$S_4^{(2)} = (\dots)^{(1)} \Psi_4^{(1)} + (\dots)^{(1)} \Psi_3^{(1)} + (\dots)^{(1)} \Psi_2^{(1)}. \quad (12)$$

The structure of $S_4^{(2)}$ explicitly illustrates how two linear parent modes couple. The first parent mode contributes the three Weyl scalars $\Psi_4^{(1)}$, $\Psi_3^{(1)}$, and $\Psi_2^{(1)}$, which are then multiplied by the terms contributed by the second parent mode (indicated in parentheses). For a given linear QNM (l, m, n, p) , the expressions for $\Psi_4^{(1)}$, $\Psi_3^{(1)}$, and $\Psi_2^{(1)}$ were analytically derived in Paper I [18], see Eqs. (38), (42), and (46) therein. An intriguing feature emerges: all three Weyl scalars contain only a single frequency component, ω_{lmn}^p , with no contribution from their mirrored counterpart, $-\bar{\omega}_{lmn}^p$. As a result, the source in Eq. (12) contains no terms resulting from the product of two mirrored frequency components.

RESULTS AND COMPARISONS

The QQNM $\begin{pmatrix} 220+ \\ 220+ \end{pmatrix}$ in the $l = m = 4$ harmonic has been extensively discussed in the literature [10–14, 18–21]. In particular, in Paper I, we found that the computed amplitude ratio, which is essentially R_{++} in Eq. (10), was smaller than those extracted from numerical relativity [13, 14]. We speculated that the difference was due to parity freedom in the linear parent modes (see Sec. VI. B in [18]). This was later confirmed in [19–21] for Schwarzschild BHs. In this work, after classifying all mode-coupling channels, we revisit the discrepancy for Kerr BHs.

As shown by the black solid lines in Fig. 1, we first compute the magnitude and phase of R_{++} as functions of the dimensionless spin χ . Good agreement is observed with the results obtained in Paper I, as represented by cyan dots. The magenta curves correspond to the results for R_{+-} . Unlike R_{++} , the magnitude of R_{+-} exhibits a weaker and non-monotonic dependence on spin, and its value is smaller than that of R_{++} by a factor of ~ 7 .

For nonprecessing binaries, the total excitability of the QQNM is characterized by R^{total} [Eq. (11)]. The gray curves in Fig. 1 show its dependence on spin. For a Schwarzschild BH, $R^{\text{total}} = 0.1534e^{-0.06787i}$, in agreement with the values reported in [19–21]. For Kerr BHs, the results (for R^{total}) extracted from numerical-relativity scattering experiments [13] are shown as green, blue, and orange dots in Fig. 1. Our findings are consistent with theirs.

We note that the values of R 's depend on the choice of angular basis — Paper I adopts spin-weighted spheroidal harmonics whereas numerical relativity simulations use

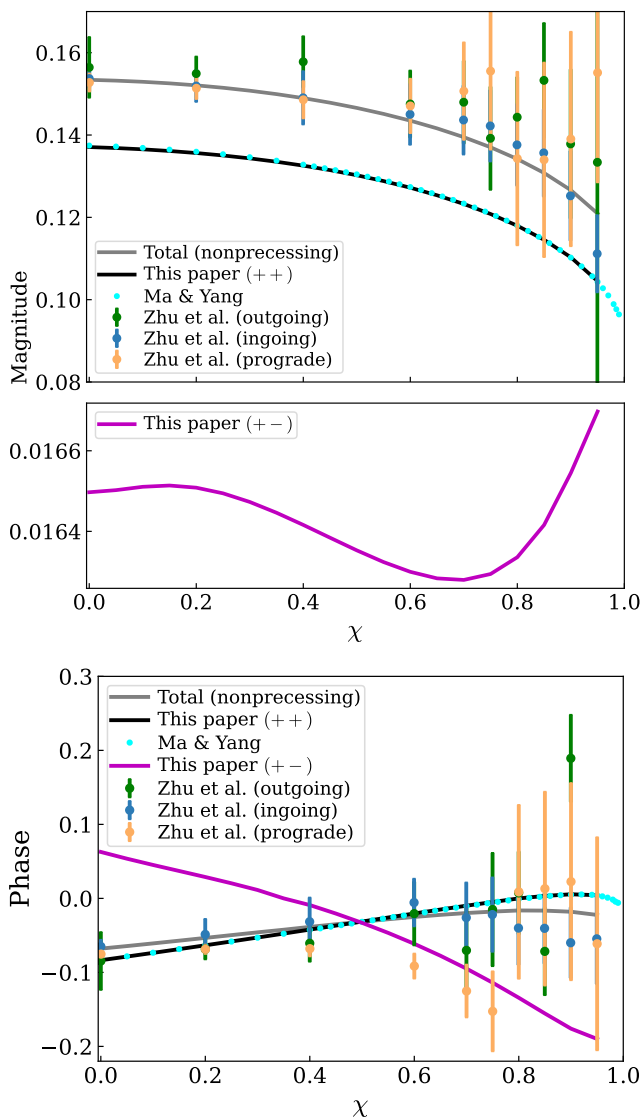


FIG. 1. A comparison between the complex contour method (cyan dots, from Paper I), time-domain numerical simulations (green, blue, and orange dots, from Zhu *et al.* [13]), and our current hyperboloidal slicing method (gray, black, and magenta curves). The gray curve represents the total amplitude ratio R^{total} for nonprecessing binaries [Eq. (11)]; the black curve corresponds to R_{++} in Eq. (9a); and the magenta curve shows R_{+-} in Eq. (9b). The mode amplitudes extracted by Zhu *et al.* [13] used spin-weighted spherical harmonics, while Paper I adopted spin-weighted spheroidal harmonics. Here we use spin-weighted spheroidal harmonics to make a fair comparison with Paper I. Results between these two angular bases differ by $\leq 1\%$ (see Supplementary Material).

spin-weighted spherical harmonics. In the Supplementary Material, we compare R across these two bases, finding that they differ by only $\sim 1\%$ even when $\chi = 0.95$. For a fair comparison with Paper I, we use spin-weighted spheroidal harmonics for the black and magenta curves in Fig. 1.

Besides $\begin{pmatrix} 220+ \\ 220+ \end{pmatrix}$, we also study five more QQNMs, including $\begin{pmatrix} 330+ \\ 220+ \end{pmatrix}$, $\begin{pmatrix} 440+ \\ 2-20- \end{pmatrix}$, $\begin{pmatrix} 220+ \\ 200+ \end{pmatrix}$, $\begin{pmatrix} 220+ \\ 200- \end{pmatrix}$, and $\begin{pmatrix} 330+ \\ 2-20- \end{pmatrix}$. In particular, we use polynomials to fit their R for different channels as functions of χ :

$$R = Ae^{i\phi}, \quad \text{with } A = \sum_{i=0}^7 A_i \chi^i, \phi = \sum_{i=0}^7 \phi_i \chi^i. \quad (13)$$

The values of the coefficients are provided in tables in the Supplementary Material.

FORECAST ON DETECTABILITY

Using the total amplitude ratio R^{total} from Eq. (11), we can estimate the SNR of various QQNMs emitted by nonprecessing binaries. To be specific, for a given binary system, we first adopt the recent surrogate model *postmerger* [8] to compute linear mode amplitudes, along with the mass and spin of the remnant BH. We then use our fitting formula for R^{total} in Eq. (13) to estimate the amplitude of the corresponding QQNMs. Finally, we follow the method outlined in [42, 46, 47] to compute their SNRs.

In the following, we focus on a 40 km CE [48] and LISA [49]. For simplicity, we average the SNRs over all angles, which yields the orthogonal condition between two antenna patterns $F_{+,x}$ for CE:

$$\langle F_{+,x}^2 \rangle = \frac{1}{5}, \quad \langle F_{+} F_x \rangle = 0.$$

For LISA, there is an additional factor of 3/2. As pointed out in Paper I, a QQNM is present in different ℓ harmonics. Its total SNR is given by given by

$$\rho = \sqrt{\sum_{\ell} \rho_{\ell,m}^2}. \quad (14)$$

In practice, we find that the first ℓ harmonic typically dominates the total SNR.

In this paper, we adopt a conservative estimate by choosing the starting time to be $10M_{\text{tot}}$ after the peak, where M_{tot} is the total mass of the binary system. Giesler *et al.* [50] demonstrate stable QNM fits at earlier times. Selecting an earlier starting time can moderately increase the SNRs, since QQNMs decay faster than linear fundamental modes.

The SNR of $\begin{pmatrix} 2, 2, 0, + \\ 2, 2, 0, + \end{pmatrix}$ was investigated in [42]. In the Supplementary Material, we present our results. A major difference between us is in the SNR's dependence on the mass ratio q . In their Fig. 6, the SNR peaks at $q \gtrsim 2$, while our more accurate calculation of the amplitude

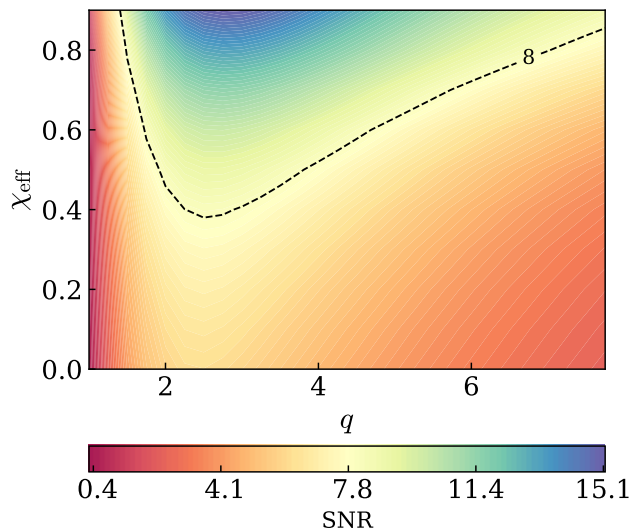
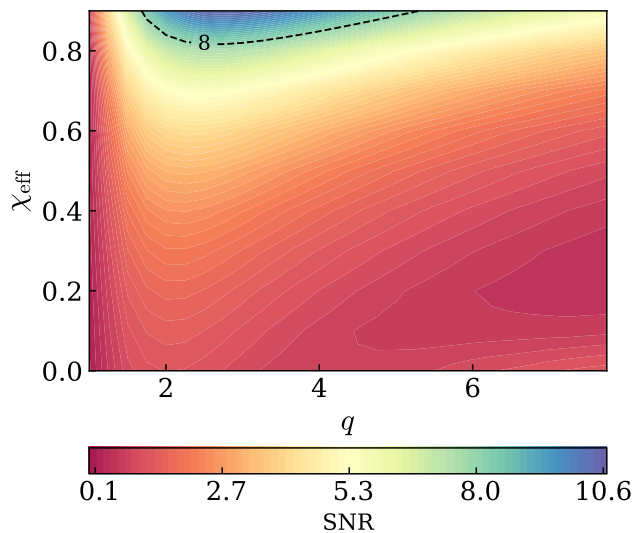
(a) $\begin{pmatrix} 3, & 3, & 0, & + \\ 2, & 2, & 0, & + \end{pmatrix}$ (b) $\begin{pmatrix} 3, & 3, & 0, & + \\ 2, & -2, & 0, & - \end{pmatrix}$

FIG. 2. The SNR dependence of two QQNM, $\begin{pmatrix} 3, & 3, & 0, & + \\ 2, & 2, & 0, & + \end{pmatrix}$, and $\begin{pmatrix} 3, & 3, & 0, & + \\ 2, & -2, & 0, & - \end{pmatrix}$, on progenitor binaries' mass ratio q and effective spin χ_{eff} . The systems have a total mass of $100M_{\odot}$ and a luminosity distance of 410 Mpc. CE sensitivity is used.

ratio shows a monotonic decrease with q . Therefore, the golden binary for detecting the QQNM is an equal-mass system with maximally positive spins.

The QQNM $\begin{pmatrix} 3, & 3, & 0, & + \\ 2, & 2, & 0, & + \end{pmatrix}$ was also identified in numerical relativity waveforms. In Fig. 2a, we present its SNR dependence on the mass ratio q and the effective inspiral spin χ_{eff} . For simplicity, we assume both component spins $\chi_{1,2}$ are equal, namely $\chi_1 = \chi_2 = \chi_{\text{eff}}$. The

optimal binary configuration is $q \sim 2.75$ with maximally positive χ_{eff} . By setting the total binary mass M_{tot} to $100M_{\odot}$, and the luminosity distance D_L to 410 Mpc, the SNR detected by CE can exceed 8 for some parameter space. With LISA, the SNR dependence on q and χ_{eff} remains the same. Assuming $M_{\text{tot}} = 8 \times 10^6 M_{\odot}$ and a redshift of 1, we find its SNR ranges from 16 to 653. The corresponding plot is available in the Supplementary Material.

The QQNM $\begin{pmatrix} 3, & 3, & 0, & + \\ 2, & -2, & 0, & - \end{pmatrix}$ is weaker. Comparing to $\begin{pmatrix} 3, & 3, & 0, & + \\ 2, & 2, & 0, & + \end{pmatrix}$, this QQNM has a smaller frequency and appears in the ($\ell \geq 2, m = 1$) harmonics. As shown in Fig. 2b, its SNR still peaks at $q \sim 2.75$ with maximally positive χ_{eff} . Using the same binaries, the SNR ranges from 0.1 to 10.6 for CE, and from 0.5 to 59.8 for LISA (see the LISA plot in the Supplementary Material).

Here we focus on two typical binary systems for CE and LISA by fixing their M_{tot} and D_L . The impact of M_{tot} on SNR is two-fold: (1) it scales the overall strain linearly; and (2) it sets the central frequency of a QQNM. In the Supplementary Material, we show how the SNR of $\begin{pmatrix} 3, & 3, & 0, & + \\ 2, & -2, & 0, & - \end{pmatrix}$ changes with M_{tot} . For CE, SNR increases monotonically from 0.6 to 30 over $M_{\text{tot}} \in [20, 200]M_{\odot}$, while for LISA, it reaches a maximum for $M_{\text{tot}} = 5.3 \times 10^6 M_{\odot}$, with a value of 64.

DISCUSSION

Together with Paper I, we have presented two independent frequency-domain methods for analyzing QQNM — the complex contour technique and the hyperboloidal slicing approach. Both methods produce consistent results for R_{++} of $\begin{pmatrix} 220+ \\ 220+ \end{pmatrix}$. We have also classified the four possible coupling channels for a QQNM. Notably, the coupling between two mirrored modes (labeled by $--$) vanishes exactly. After accounting for all coupling channels in systems with reflection symmetry, our results for Kerr BHs match those from numerical simulations and time-domain fits.

We have performed a SNR survey on various QQNM for nonprecessing binaries. Besides the known mode $\begin{pmatrix} 220+ \\ 220+ \end{pmatrix}$, we considered two more: $\begin{pmatrix} 3, & 3, & 0, & + \\ 2, & -2, & 0, & - \end{pmatrix}$ and $\begin{pmatrix} 3, & 3, & 0, & + \\ 2, & 2, & 0, & + \end{pmatrix}$. For an event with $M_{\text{tot}} = 100M_{\odot}$ and $D_L = 410$ Mpc, the SNR for CE may reach $\mathcal{O}(8)$ for binaries with $\chi_{\text{eff}} > 0.6$ and $q \in (2, 5)$. For SgrA*-like binaries ($M_{\text{tot}} = 8 \times 10^6 M_{\odot}$) at a redshift of 1, LISA's SNR may reach $\mathcal{O}(10^2)$. We expect LISA to detect additional QQNM. A more detailed survey is left for future work. Future studies could also explore precessing bina-

ries, where QQNM excitation may encode richer information about linear parent modes and progenitors' parity. It would be interesting to explore how to decipher the information from QQNM amplitudes.

Although this work, together with Paper I, has offered a comprehensive discussion on QQNMs, a complete account of all second-order effects has yet to be provided. Intriguing avenues for future study include the memory effect of a QNM, quadratic tails, and the possibility of resolving the nonlinear tails from numerical simulations, using techniques such as Cauchy-characteristic matching [51].

ACKNOWLEDGMENTS

We thank Hengrui Zhu for sharing the data in Fig. 1. We thank Andrew Spiers for pointing out the difference between the Campanelli–Lousto–Teukolsky equation and the reduced second-order Teukolsky equation. Research at Perimeter Institute is supported in part by the Government of Canada through the Department of Innovation, Science and Economic Development and by the Province of Ontario through the Ministry of Colleges and Universities. N.K. is supported by the Natural Science and Engineering Council of Canada.

* hyangdoa@tsinghua.edu.cn

- [1] E. Berti, V. Cardoso, and A. O. Starinets, Quasinormal modes of black holes and black branes, *Class. Quant. Grav.* **26**, 163001 (2009), [arXiv:0905.2975 \[gr-qc\]](https://arxiv.org/abs/0905.2975).
- [2] R. A. Konoplya and A. Zhidenko, Quasinormal modes of black holes: From astrophysics to string theory, *Rev. Mod. Phys.* **83**, 793 (2011), [arXiv:1102.4014 \[gr-qc\]](https://arxiv.org/abs/1102.4014).
- [3] E. Berti, K. Yagi, H. Yang, and N. Yunes, Extreme Gravity Tests with Gravitational Waves from Compact Binary Coalescences: (II) Ringdown, *Gen. Rel. Grav.* **50**, 49 (2018), [arXiv:1801.03587 \[gr-qc\]](https://arxiv.org/abs/1801.03587).
- [4] L. London, D. Shoemaker, and J. Healy, Modeling ringdown: Beyond the fundamental quasinormal modes, *Phys. Rev. D* **90**, 124032 (2014), [Erratum: *Phys.Rev.D* 94, 069902 (2016)], [arXiv:1404.3197 \[gr-qc\]](https://arxiv.org/abs/1404.3197).
- [5] L. T. London, Modeling ringdown. II. Aligned-spin binary black holes, implications for data analysis and fundamental theory, *Phys. Rev. D* **102**, 084052 (2020), [arXiv:1801.08208 \[gr-qc\]](https://arxiv.org/abs/1801.08208).
- [6] S. A. Hughes, A. Apte, G. Khanna, and H. Lim, Learning about black hole binaries from their ringdown spectra, *Phys. Rev. Lett.* **123**, 161101 (2019), [arXiv:1901.05900 \[gr-qc\]](https://arxiv.org/abs/1901.05900).
- [7] M. H.-Y. Cheung, E. Berti, V. Baibhav, and R. Cotesta, Extracting linear and nonlinear quasinormal modes from black hole merger simulations, *Phys. Rev. D* **109**, 044069 (2024), [Erratum: *Phys.Rev.D* 110, 049902 (2024)], [arXiv:2310.04489 \[gr-qc\]](https://arxiv.org/abs/2310.04489).
- [8] C. Pacilio, S. Bhagwat, F. Nobili, and D. Gerosa, postmerger: A flexible mapping of ringdown amplitudes for non-precessing binary black holes, (2024), [arXiv:2408.05276 \[gr-qc\]](https://arxiv.org/abs/2408.05276).
- [9] L. Magaña Zertuche *et al.*, High-Precision Ringdown Surrogate Model for Non-Precessing Binary Black Holes, (2024), [arXiv:2408.05300 \[gr-qc\]](https://arxiv.org/abs/2408.05300).
- [10] K. Mitman *et al.*, Nonlinearities in Black Hole Ringdowns, *Phys. Rev. Lett.* **130**, 081402 (2023), [arXiv:2208.07380 \[gr-qc\]](https://arxiv.org/abs/2208.07380).
- [11] M. H.-Y. Cheung *et al.*, Nonlinear Effects in Black Hole Ringdown, *Phys. Rev. Lett.* **130**, 081401 (2023), [arXiv:2208.07374 \[gr-qc\]](https://arxiv.org/abs/2208.07374).
- [12] S. Ma, K. Mitman, L. Sun, N. Deppe, F. Hébert, L. E. Kidder, J. Moxon, W. Throwe, N. L. Vu, and Y. Chen, Quasinormal-mode filters: A new approach to analyze the gravitational-wave ringdown of binary black-hole mergers, *Phys. Rev. D* **106**, 084036 (2022), [arXiv:2207.10870 \[gr-qc\]](https://arxiv.org/abs/2207.10870).
- [13] H. Zhu *et al.*, Nonlinear effects in black hole ringdown from scattering experiments: Spin and initial data dependence of quadratic mode coupling, *Phys. Rev. D* **109**, 104050 (2024), [arXiv:2401.00805 \[gr-qc\]](https://arxiv.org/abs/2401.00805).
- [14] J. Redondo-Yuste, G. Carullo, J. L. Ripley, E. Berti, and V. Cardoso, Spin dependence of black hole ringdown nonlinearities, *Phys. Rev. D* **109**, L101503 (2024), [arXiv:2308.14796 \[gr-qc\]](https://arxiv.org/abs/2308.14796).
- [15] H. Zhu *et al.*, Imprints of Changing Mass and Spin on Black Hole Ringdown, (2024), [arXiv:2404.12424 \[gr-qc\]](https://arxiv.org/abs/2404.12424).
- [16] T. May, S. Ma, J. L. Ripley, and W. E. East, Nonlinear effect of absorption on the ringdown of a spinning black hole, *Phys. Rev. D* **110**, 084034 (2024), [arXiv:2405.18303 \[gr-qc\]](https://arxiv.org/abs/2405.18303).
- [17] N. Khera, A. Ribes Metidieri, B. Bonga, X. Jiménez Forteza, B. Krishnan, E. Poisson, D. Pook-Kolb, E. Schnetter, and H. Yang, Nonlinear Ringdown at the Black Hole Horizon, *Phys. Rev. Lett.* **131**, 231401 (2023), [arXiv:2306.11142 \[gr-qc\]](https://arxiv.org/abs/2306.11142).
- [18] S. Ma and H. Yang, Excitation of quadratic quasinormal modes for Kerr black holes, *Phys. Rev. D* **109**, 104070 (2024), [arXiv:2401.15516 \[gr-qc\]](https://arxiv.org/abs/2401.15516).
- [19] B. Bucciotti, L. Juliano, A. Kuntz, and E. Trinchineri, Quadratic Quasi-Normal Modes of a Schwarzschild Black Hole, (2024), [arXiv:2405.06012 \[gr-qc\]](https://arxiv.org/abs/2405.06012).
- [20] B. Bucciotti, L. Juliano, A. Kuntz, and E. Trinchineri, Amplitudes and polarizations of quadratic quasi-normal modes for a Schwarzschild black hole, *JHEP* **09**, 119, [arXiv:2406.14611 \[hep-th\]](https://arxiv.org/abs/2406.14611).
- [21] P. Bourg, R. Panosso Macedo, A. Spiers, B. Leather, B. Bonga, and A. Pound, Quadratic quasi-normal mode dependence on linear mode parity, (2024), [arXiv:2405.10270 \[gr-qc\]](https://arxiv.org/abs/2405.10270).
- [22] J. Redondo-Yuste, D. Pereñíguez, and V. Cardoso, Ringdown of a dynamical spacetime, *Phys. Rev. D* **109**, 044048 (2024), [arXiv:2312.04633 \[gr-qc\]](https://arxiv.org/abs/2312.04633).
- [23] L. Sberna, P. Bosch, W. E. East, S. R. Green, and L. Lehner, Nonlinear effects in the black hole ringdown: Absorption-induced mode excitation, *Phys. Rev. D* **105**, 064046 (2022), [arXiv:2112.11168 \[gr-qc\]](https://arxiv.org/abs/2112.11168).
- [24] J. Ben Achour and H. Roussille, Quadratic perturbations of the Schwarzschild black hole: the algebraically special sector, *JCAP* **07**, 085, [arXiv:2406.08159 \[gr-qc\]](https://arxiv.org/abs/2406.08159).
- [25] D. Perrone, T. Barreira, A. Kehagias, and A. Riotto, Non-linear black hole ringdowns: An analytical approach, *Nucl. Phys. B* **999**, 116432 (2024), [arXiv:2308.15886 \[gr-qc\]](https://arxiv.org/abs/2308.15886).

- [26] A. Kehagias, D. Perrone, A. Riotto, and F. Riva, Explaining nonlinearities in black hole ringdowns from symmetries, *Phys. Rev. D* **108**, L021501 (2023), [arXiv:2301.09345 \[gr-qc\]](https://arxiv.org/abs/2301.09345).
- [27] G. Carullo, W. Del Pozzo, and J. Veitch, Observational Black Hole Spectroscopy: A time-domain multi-mode analysis of GW150914, *Phys. Rev. D* **99**, 123029 (2019), [Erratum: *Phys.Rev.D* 100, 089903 (2019)], [arXiv:1902.07527 \[gr-qc\]](https://arxiv.org/abs/1902.07527).
- [28] M. Isi and W. M. Farr, Analyzing black-hole ringdowns, (2021), [arXiv:2107.05609 \[gr-qc\]](https://arxiv.org/abs/2107.05609).
- [29] H. Siegel, M. Isi, and W. M. Farr, Analyzing black-hole ringdowns II: data conditioning, (2024), [arXiv:2410.02704 \[gr-qc\]](https://arxiv.org/abs/2410.02704).
- [30] C. D. Capano, M. Cabero, J. Westerweck, J. Abedi, S. Kastha, A. H. Nitz, Y.-F. Wang, A. B. Nielsen, and B. Krishnan, Multimode Quasinormal Spectrum from a Perturbed Black Hole, *Phys. Rev. Lett.* **131**, 221402 (2023), [arXiv:2105.05238 \[gr-qc\]](https://arxiv.org/abs/2105.05238).
- [31] Y.-F. Wang, C. D. Capano, J. Abedi, S. Kastha, B. Krishnan, A. B. Nielsen, A. H. Nitz, and J. Westerweck, A gating-and-inpainting perspective on GW150914 ringdown overtone: understanding the data analysis systematics, (2023), [arXiv:2310.19645 \[gr-qc\]](https://arxiv.org/abs/2310.19645).
- [32] S. Ma, L. Sun, and Y. Chen, Using rational filters to uncover the first ringdown overtone in GW150914, *Phys. Rev. D* **107**, 084010 (2023), [arXiv:2301.06639 \[gr-qc\]](https://arxiv.org/abs/2301.06639).
- [33] S. Ma, L. Sun, and Y. Chen, Black Hole Spectroscopy by Mode Cleaning, *Phys. Rev. Lett.* **130**, 141401 (2023), [arXiv:2301.06705 \[gr-qc\]](https://arxiv.org/abs/2301.06705).
- [34] M. Campanelli and C. O. Lousto, Second order gauge invariant gravitational perturbations of a Kerr black hole, *Phys. Rev. D* **59**, 124022 (1999), [arXiv:gr-qc/9811019](https://arxiv.org/abs/gr-qc/9811019).
- [35] S. R. Green, S. Hollands, and P. Zimmerman, Teukolsky formalism for nonlinear Kerr perturbations, *Class. Quant. Grav.* **37**, 075001 (2020), [arXiv:1908.09095 \[gr-qc\]](https://arxiv.org/abs/1908.09095).
- [36] A. R. C. Spiers, *Second-order gravitational self-force in Kerr spacetime*, Ph.D. thesis, University of Southampton (2022).
- [37] A. Zenginoglu, A Geometric framework for black hole perturbations, *Phys. Rev. D* **83**, 127502 (2011), [arXiv:1102.2451 \[gr-qc\]](https://arxiv.org/abs/1102.2451).
- [38] A. Zenginoglu, Hyperboloidal foliations and scri-fixing, *Class. Quant. Grav.* **25**, 145002 (2008), [arXiv:0712.4333 \[gr-qc\]](https://arxiv.org/abs/0712.4333).
- [39] R. Panosso Macedo and A. Zenginoglu, Hyperboloidal Approach to Quasinormal Modes, (2024), [arXiv:2409.11478 \[gr-qc\]](https://arxiv.org/abs/2409.11478).
- [40] J. Baker *et al.*, The Laser Interferometer Space Antenna: Unveiling the Millihertz Gravitational Wave Sky, (2019), [arXiv:1907.06482 \[astro-ph.IM\]](https://arxiv.org/abs/1907.06482).
- [41] M. Evans *et al.*, A Horizon Study for Cosmic Explorer: Science, Observatories, and Community, (2021), [arXiv:2109.09882 \[astro-ph.IM\]](https://arxiv.org/abs/2109.09882).
- [42] S. Yi, A. Kuntz, E. Barausse, E. Berti, M. H.-Y. Cheung, K. Kritos, and A. Maselli, Nonlinear quasinormal mode detectability with next-generation gravitational wave detectors, *Phys. Rev. D* **109**, 124029 (2024), [arXiv:2403.09767 \[gr-qc\]](https://arxiv.org/abs/2403.09767).
- [43] J. L. Jaramillo, R. Panosso Macedo, and L. Al Sheikh, Pseudospectrum and Black Hole Quasinormal Mode Instability, *Phys. Rev. X* **11**, 031003 (2021), [arXiv:2004.06434 \[gr-qc\]](https://arxiv.org/abs/2004.06434).
- [44] J. L. Ripley, Computing the quasinormal modes and eigenfunctions for the Teukolsky equation using horizon penetrating, hyperboloidally compactified coordinates, *Class. Quant. Grav.* **39**, 145009 (2022), [arXiv:2202.03837 \[gr-qc\]](https://arxiv.org/abs/2202.03837).
- [45] D. K. Zhang, Multifloats.jl, <https://github.com/dzhang314/MultiFloats.jl>.
- [46] E. E. Flanagan and S. A. Hughes, Measuring gravitational waves from binary black hole coalescences: 1. Signal-to-noise for inspiral, merger, and ringdown, *Phys. Rev. D* **57**, 4535 (1998), [arXiv:gr-qc/9701039](https://arxiv.org/abs/gr-qc/9701039).
- [47] E. Berti, V. Cardoso, and C. M. Will, On gravitational-wave spectroscopy of massive black holes with the space interferometer LISA, *Phys. Rev. D* **73**, 064030 (2006), [arXiv:gr-qc/0512160](https://arxiv.org/abs/gr-qc/0512160).
- [48] M. Evans *et al.*, Cosmic Explorer: A Submission to the NSF MPSAC ngGW Subcommittee, (2023), [arXiv:2306.13745 \[astro-ph.IM\]](https://arxiv.org/abs/2306.13745).
- [49] T. Robson, N. J. Cornish, and C. Liu, The construction and use of LISA sensitivity curves, *Class. Quant. Grav.* **36**, 105011 (2019), [arXiv:1803.01944 \[astro-ph.HE\]](https://arxiv.org/abs/1803.01944).
- [50] M. Giesler, S. Ma, K. Mitman, N. Oshita, and S. A. Teukolsky, Overtones and Nonlinearities in Binary Black Hole Ringdowns (2024, in preparation).
- [51] S. Ma *et al.*, Fully relativistic three-dimensional Cauchy-characteristic matching for physical degrees of freedom, *Phys. Rev. D* **109**, 124027 (2024), [arXiv:2308.10361 \[gr-qc\]](https://arxiv.org/abs/2308.10361).
- [52] R. P. Geroch, A. Held, and R. Penrose, A space-time calculus based on pairs of null directions, *J. Math. Phys.* **14**, 874 (1973).
- [53] S. Olver and A. Townsend, A fast and well-conditioned spectral method, *SIAM Review* **55**, 462 (2013), <https://doi.org/10.1137/120865458>.
- [54] L. C. Stein, qnm: A Python package for calculating Kerr quasinormal modes, separation constants, and spherical-spheroidal mixing coefficients, *J. Open Source Softw.* **4**, 1683 (2019), [arXiv:1908.10377 \[gr-qc\]](https://arxiv.org/abs/1908.10377).
- [55] K. M. Huffman and B. D. Wandelt, Fast and exact spin-s spherical harmonic transforms, *The Astrophysical Journal Supplement Series* **189**, 255 (2010).
- [56] M. Boyle, L. E. Kidder, S. Ossokine, and H. P. Pfeiffer, Gravitational-wave modes from precessing black-hole binaries, (2014), [arXiv:1409.4431 \[gr-qc\]](https://arxiv.org/abs/1409.4431).
- [57] D. J. Vickers and G. B. Cook, Understanding solutions of the angular Teukolsky equation in the prolate asymptotic limit, *Phys. Rev. D* **106**, 104037 (2022), [arXiv:2208.06259 \[gr-qc\]](https://arxiv.org/abs/2208.06259).

SUPPLEMENTARY MATERIAL

Description of the numerical code

As discussed before, we solve the nonlinear Teukolsky equations on a hyperboloidal slicing. We use identical

coordinates as in [44]. Namely, for the Kerr metric

$$ds^2 = - \left(1 - \frac{2Mr}{\Sigma}\right) dt^2 - \frac{4Mar \sin^2 \theta}{\Sigma} dt d\phi + \frac{\Sigma}{\Delta} dr^2 + \Sigma d\theta^2 + \left(r^2 + a^2 + \frac{2Ma^2 r \sin^2 \theta}{\Sigma}\right) \sin^2 \theta d\phi^2, \quad (15)$$

where $\Sigma = r^2 + a^2 \cos^2 \theta$ and $\Delta = r^2 - 2Mr + a^2$, we change the coordinates (t, r, ϕ) to (T, R, Φ) where

$$dT = dt + \frac{r^2 + a^2}{\Delta} dr - 2 \left(1 + \frac{2M}{r}\right) dr, \quad (16a)$$

$$d\Phi = d\phi + \frac{adr}{\Delta}, \quad (16b)$$

$$R = \frac{1}{r}, \quad (16c)$$

and where the coordinate θ remains unchanged. Note that the coordinates T and Φ are chosen such that they are well-defined at the horizon. Furthermore, $T = \text{const}$ slices are hyperboloidal, namely they penetrate the horizon and null infinity, and become light-like in the $r \rightarrow \infty$ limit. The coordinate R is chosen to compactify the space-time radially onto a finite domain.

The principal null tetrad must also be chosen to be regular at both the horizon and null-infinity. While the Kinnersley tetrad is regular at null-infinity, it is not a good choice at the horizon. Therefore, we choose the tetrad $(\ell^a, n^a, m^a, \bar{m}^a)$ given by

$$\ell^a = \frac{\Delta}{2r^2} \ell_K^a, \quad (17)$$

$$n^a = \frac{2r^2}{\Delta} n_K^a, \quad (18)$$

$$m^a = m_K^a, \quad (19)$$

where $(\ell_K^a, n_K^a, m_K^a, \bar{m}_K^a)$ is the Kinnersley null tetrad.

Under these coordinates and conventions the spin- s radial Teukolsky equation for the spin- s field ψ_s , with $\psi_s = R^{1+2s} \psi_s^\circ$ becomes

$$\alpha \psi_s^\circ + \beta \partial_R \psi_s^\circ - (1 - 2MR^2 + a^2 R^2) R^2 \partial_R^2 \psi_s^\circ = -(\Lambda/2 + 1) \psi_s^\circ, \quad (20)$$

where Λ is the separation constant of the angular Teukolsky equation and α and β are given by

$$\begin{aligned} \alpha &= a^2 R^2 (8M^2 \omega^2 + 6iM\omega - 1) \\ &\quad - R(4M\omega + i) (-a(a\omega + m) + 4M^2 \omega + iM(s + 1)) \\ &\quad + \frac{1}{2} \omega^2 (a^2 - 16M^2) + am\omega + s \left(-\frac{1}{2} + 2iM\omega\right), \end{aligned} \quad (21)$$

$$\begin{aligned} \beta &= 2a^2 R^3 (-1 + 2iM\omega) + R(-s - 1) + i\omega \\ &\quad + R^2 (ia(a\omega + m) - 8iM^2 \omega + M(s + 3)). \end{aligned} \quad (22)$$

For instance, for the Teukolsky equation of Ψ_4 we have $s = -2$ and $\psi_s = \zeta^4 \Psi_4$, where $\zeta = r + ia \cos \theta$. Whereas for Ψ_0 we have $s = 2$ and $\psi_s = \Psi_0$.

To solve the second-order Teukolsky equation, we need the reconstructed metric at linear order to compute the source term. We obtain the metric by first solving for the outgoing radiation gauge (ORG) Hertz potential and then performing metric reconstruction. We use the ORG because the ingoing radiation gauge is not well-behaved at null infinity. To solve the Hertz potential Φ we note that $\zeta^{-4} \Phi$ satisfies the $s = 2$ Teukolsky equation, where $\zeta = r - ia \cos \theta$. Consequently, we need to solve the $s = 2$ radial Teukolsky equation to get a solution for the Hertz potential that corresponds to QNMs for the reconstructed metric.

The metric, reconstructed from the Hertz potential, in GHP notation [52], is given by

$$\begin{aligned} h_{ab} &= -\frac{1}{2} \left[n_a n_b (\bar{\partial}' - \tau') (\bar{\partial}' - \tau') \right. \\ &\quad + \bar{m}_a \bar{m}_b (\rho' - \rho') (\rho' - \rho') \\ &\quad - n_{(a} \bar{m}_{b)} \left((\bar{\partial}' - \tau' + \bar{\tau}) (\rho' - \rho') \right. \\ &\quad \left. \left. + (\rho' - \rho' + \bar{\rho}') (\bar{\partial}' - \tau') \right) \right] \Phi + c.c. \end{aligned} \quad (23)$$

Evidently from (23) the gravitational strain $h = h_{ab} \bar{m}^a \bar{m}^b$ (and therefore Ψ_4) only has contributions from $\bar{\Phi}$, instead of Φ directly. Consequently, to get a QNM frequency $\omega_{\ell mn}^p$ in h , we must have the frequency $-\bar{\omega}_{\ell mn}^p$ and azimuthal quantum number $-m$ in the Hertz potential. Note however that the outgoing and ingoing boundary conditions do not get mixed under complex conjugation or derivatives, therefore if the strain h satisfies purely outgoing boundary conditions, so does the Hertz potential $\bar{\Phi}$. Therefore, we find the QNM solutions for the mode (ℓ, m, n, p) by finding outgoing solutions to the Hertz potential $\bar{\Phi}$ with azimuthal quantum number $-m$ and frequency $-\bar{\omega}_{\ell mn}^p$.

We implement this numerically using the spectral method following the procedure in [44], which we summarize below. We first separate the Hertz potential into radial and angular parts

$$\bar{\Phi} = R \mathcal{R}(R) \mathcal{S}(\theta, \Phi) e^{-i\omega T}, \quad (24)$$

which can be done because of the separation of the Teukolsky equation. Note we have also separated the leading order fall off at null infinity $\sim R$ so that \mathcal{R} is $\mathcal{O}(1)$ at null infinity. Then, the radial and angular functions \mathcal{R} and \mathcal{S} can be expanded into Chebyshev polynomials $T_n(x)$ and the spin-weighted spherical harmonics ${}_2Y_{\ell m}(\theta, \phi)$ respectively.

$$\mathcal{R}(R) = \sum_{n=0}^{\infty} c_n T_n(1 - 2Rr_+), \quad (25)$$

$$\mathcal{S}(\theta, \Phi) = \sum_{\ell} s_{\ell} {}_2Y_{\ell m}(\theta, \Phi). \quad (26)$$

The outgoing boundary conditions at the horizon and null infinity imply that \mathcal{R} is analytic [44] at the boundary and thus c_n falls exponentially with n , whereas for the ingoing boundary conditions, the c_n falls faster than any polynomial because the solution is smooth, yet it falls slower than an exponential. Thus, just as in Leaver's method the QNM solutions are the minimal solution of the radial equation. Then, if we impose the conditions $c_{n_{\max}+1} = c_{n_{\max}+2} = 0$ for a large enough n_{\max} and solve for the truncated coefficients $c_0 \dots c_{n_{\max}}$, the solution will be dominated by outgoing solutions just as for Leaver's method (if a non-zero solution exists for that frequency). Additionally, we can also truncate the angular expansion at some ℓ_{\max} for numerical purposes.

The truncated Radial and Angular Teukolsky equations now turn into matrix eigenvalue problems, with the separation constant Λ related to their respective eigenvalues. We change the basis after differentiating to Gegenbauer polynomials to improve the conditioning of the linear problem [53]. For generic frequencies, the two equations will not give the same value of Λ , however for QNMs they do. Therefore, following [44], we find QNMs by minimizing the difference between the separation constants obtained from the radial and angular equations, using the frequencies from the `qnm` package as a good initial guess [54]. This gives us the Hertz potential as a series in Chebyshev and spin-weighted spherical harmonics. We do this for both pairs of linear modes with frequencies ω_1 and ω_2 we want to compute the quadratic contribution to and take their linear combination.

From the Hertz potential, we use (23) to obtain the linearized metric. Here derivatives become linear operators that can be applied to the spectral coefficients. To perform multiplication, we first transform the spectral data into a grid of 2d collocation points by performing the fast discrete cosine transform on the radial direction, and an adaptation of the fast spin-weighted spherical harmonics transform described in [55] for the angular direction, where the grid in the ϕ direction is not computed because our fields have a fixed azimuthal quantum number m . Then after point-wise multiplication on the grid, we transform back to the spectral domain using the inverse fast discrete cosine transform and the inverse fast spin-weighted spherical harmonics transform. We keep track of the fall-off in R of all the terms and perform spectral expansion of the $\mathcal{O}(1)$ parts.

Finally, using the metric, we compute the Einstein tensor $G_{ab}^{(2)}[h_{ab}, h_{ab}]$ quadratic in h_{ab} . Here again, we perform multiplications by transforming to a 2d grid of points. As discussed in the main text, $T_{ab} = -G_{ab}^{(2)}[h_{ab}, h_{ab}]/8\pi$ acts as the effective stress-energy tensor for the next order. The Teukolsky equation derived from this equation is the reduced Teukolsky equation [36], because it only gives the second order Ψ_4 computed linearly from $h_{ab}^{(2)}$ and does not include contributions from

the quadratic terms in $h_{ab}^{(1)}$. However, it can be checked that in the outgoing radiation gauge this contribution vanishes, and therefore the reduced Teukolsky equation gives the full Ψ_4 . From this effective stress-energy tensor we can compute the source term S for the $s = -2$ reduced Teukolsky equation using

$$S = \frac{1}{2}(\partial' - \bar{\tau} - 4\tau')[(\mathfrak{p}' - 2\bar{\rho}')T_{n\bar{m}} - (\partial' - \bar{\tau})T_{n\bar{m}}] + \frac{1}{2}(\mathfrak{p}' - 4\rho' - \bar{\rho}')[(\partial' - 2\bar{\tau})T_{n\bar{m}} - (\mathfrak{p}' - \bar{\rho}')T_{\bar{m}\bar{m}}], \quad (27)$$

and then solving the sourced Teukolsky equation

$$\mathcal{T}[\Psi_4] = S. \quad (28)$$

The resulting source term has frequencies $\omega_1 + \omega_2$, $\omega_1 - \bar{\omega}_2$ and $-\bar{\omega}_1 + \omega_2$. As discussed in the main text, the contribution to the $-\bar{\omega}_1 - \bar{\omega}_2$ vanishes. This gives rise to three frequencies ω_{quad} in the second order Ψ_4 , and we solve each separately. This could be done by simply getting the Teukolsky operator in matrix form on the spectral coefficients and inverting it. However, we can utilize the separation of the Teukolsky equation to invert it directly. We first re-expand the source term in a basis of Spheroidal harmonics ${}_{-2}S_{\ell m_{\text{quad}}}(\theta, \phi; a\omega_{\text{quad}})$ using the procedure described in [18]. Then, the coefficients of the spheroidal harmonics satisfy the radial Teukolsky equation (20) with a source. This reduces the dimensions of the problem, leading to faster computations. After separating the leading order fall-off in R , the radial operator in (20) can be expressed as a lower dimensional matrix. Then, the spheroidal harmonic component of S gives us the source term for the matrix equation. Finally, by solving the matrix equation we get a solution to the quadratic Ψ_4 from the horizon to null infinity. We can similarly solve for the reduced Ψ_0 as well. However for Ψ_0 the quadratic terms from the $h_{ab}^{(1)}$ can contribute. This can be added to the reduced Ψ_0 by using the $h_{ab}^{(1)}$ from the metric reconstruction. In this paper, we only report the reduced Ψ_0 which depends linearly on $h_{ab}^{(2)}$.

Coupling strength for selected quadratic channels

We compute the amplitude ratio R for five QQNMs, including $\begin{pmatrix} 220+ \\ 220+ \end{pmatrix}$, $\begin{pmatrix} 330+ \\ 220+ \end{pmatrix}$, $\begin{pmatrix} 440+ \\ 2-20- \end{pmatrix}$, $\begin{pmatrix} 220+ \\ 200+ \end{pmatrix}$, and $\begin{pmatrix} 330+ \\ 2-20- \end{pmatrix}$. We then fit their magnitudes and phases using polynomials as functions of χ :

$$R = Ae^{i\phi}, \quad \text{with } A = \sum_{i=0}^7 A_i \chi^i, \quad \phi = \sum_{i=0}^7 \phi_i \chi^i. \quad (29)$$

The values of A_i 's and ϕ_i 's are listed in Table I and II, respectively. Spin-weighted spherical harmonics are used as the angular basis.

QQNM	Child Harmonic (ℓ, m)	Channel	A_0	A_1	A_2	A_3	A_4	A_5	A_6	A_7
$\begin{pmatrix} 2 & 2 & 0 & + \\ 2 & 2 & 0 & + \end{pmatrix}$	(4, 4)	(+, +)	0.1371	-0.005585	0.01943	-0.2619	0.8867	-1.592	1.412	-0.4997
		(+, -)	0.0165	-0.0001457	0.006129	-0.04495	0.1308	-0.1975	0.1517	-0.04564
$\begin{pmatrix} 3 & 3 & 0 & + \\ 2 & 2 & 0 & + \end{pmatrix}$	(5, 5)	(+, +)	0.3608	0.02932	0.07302	-0.8313	2.784	-4.999	4.432	-1.568
		(+, -)	0.05032	0.003027	0.01122	-0.1226	0.4119	-0.7302	0.6395	-0.2213
		(+, -)	0.009198	0.001532	-0.0002162	0.003541	-0.0189	0.04243	-0.04322	0.01752
$\begin{pmatrix} 4 & 4 & 0 & + \\ 2 & -2 & 0 & - \end{pmatrix}$	(2, 2)	(+, +)	0.0289	0.01489	0.0405	-0.3652	1.065	-1.568	1.171	-0.3534
		(+, -)	0.4171	0.01512	0.05565	-0.5754	1.934	-3.438	3.019	-1.052
		(-, +)	0.01829	0.02588	-0.06939	0.05871	0.1518	-0.3899	0.3364	-0.101
$\begin{pmatrix} 2 & 2 & 0 & + \\ 2 & 0 & 0 & + \end{pmatrix}$	(2, 2)	(+, +)	0.05129	0.002777	-0.03533	0.2996	-1.03	1.837	-1.623	0.569
		(+, -)	0.002267	0.007251	-0.04791	0.3853	-1.324	2.365	-2.092	0.7351
		(-, +)	0.002277	-0.002326	-0.0002231	0.002508	-0.00836	0.01393	-0.01062	0.002952
$\begin{pmatrix} 3 & 3 & 0 & + \\ 2 & -2 & 0 & - \end{pmatrix}$	(2, 1)	(+, +)	1.554	-12.84	50.72	-123.4	195.0	-193.3	108.1	-25.79
		(+, -)	0.1214	-0.07163	-0.7033	5.926	-18.9	29.89	-23.39	7.367
		(-, +)	1.359	-11.42	44.2	-99.21	142.2	-130.1	69.21	-16.1

TABLE I. Polynomial fit coefficients for the magnitude of R . Spin-weighted spherical harmonics are used as the angular basis.

QQNM	Child Harmonic (ℓ, m)	Channel	ϕ_0	ϕ_1	ϕ_2	ϕ_3	ϕ_4	ϕ_5	ϕ_6	ϕ_7
$\begin{pmatrix} 2 & 2 & 0 & + \\ 2 & 2 & 0 & + \end{pmatrix}$	(4, 4)	(+, +)	-0.08353	0.09268	0.1207	-0.7802	2.712	-4.846	4.292	-1.509
		(+, -)	0.0627	-0.1758	-0.1173	1.938	-8.759	16.69	-15.12	5.295
$\begin{pmatrix} 3 & 3 & 0 & + \\ 2 & 2 & 0 & + \end{pmatrix}$	(5, 5)	(+, +)	-0.1163	0.09638	0.123	-0.709	2.481	-4.433	3.927	-1.383
		(+, -)	0.1351	-0.04489	-0.137	0.8002	-2.83	4.876	-4.211	1.396
		(+, -)	-3.005	-0.1198	-0.101	0.4773	-2.07	3.604	-3.137	1.037
$\begin{pmatrix} 4 & 4 & 0 & + \\ 2 & -2 & 0 & - \end{pmatrix}$	(2, 2)	(+, +)	-2.897	-0.6309	5.9	-20.57	44.59	-59.43	44.04	-13.87
		(+, -)	-2.924	-0.08228	0.2784	-1.909	6.662	-11.95	10.62	-3.753
		(-, +)	3.082	-0.5622	5.915	-22.96	47.31	-53.63	32.0	-7.771
$\begin{pmatrix} 2 & 2 & 0 & + \\ 2 & 0 & 0 & + \end{pmatrix}$	(2, 2)	(+, +)	1.391	0.04503	-0.06083	0.4756	-1.594	2.739	-2.32	0.7656
		(+, -)	0.5607	0.284	-0.6156	4.681	-15.89	28.36	-25.05	8.796
		(-, +)	0.5608	-0.1216	-0.03096	-0.7142	3.298	-8.916	9.931	-4.232
$\begin{pmatrix} 3 & 3 & 0 & + \\ 2 & -2 & 0 & - \end{pmatrix}$	(2, 1)	(+, +)	-3.001	1.598	19.14	-142.2	464.0	-707.2	498.3	-130.7
		(+, -)	3.024	-0.5552	-6.804	23.97	-29.44	-2.589	26.3	-12.33
		(-, +)	0.4982	5.452	-49.14	344.5	-964.2	1285.0	-828.4	208.5

TABLE II. Polynomial fit coefficients for the phase of R . Spin-weighted spherical harmonics are used as the angular basis.

The value of R depends on the choice of angular basis, whether using spin-weighted spherical or spheroidal harmonics. In Fig. 3, we compare R_{++} for $\begin{pmatrix} 220+ \\ 220+ \end{pmatrix}$ between the two bases. We find the results differ by $\leq 1\%$ even for dimensionless spins as large as 0.95. Nonetheless, there are modes where the difference is significant.

The QQNM $\begin{pmatrix} 220+ \\ 200- \end{pmatrix}$ needs more attention. As shown in Fig. 4, our code encounters issues as $\chi \rightarrow 0$, and the value of R_{++} diverges. This occurs because, in the Schwarzschild limit, the QQNM becomes purely decaying. Its pole coincides with the branch cut along the imaginary axis. This feature indicates that memory-type quadratic effects require special treatment, which we leave for future work.

Furthermore, the numerical code can also compute the amplitude of the nonlinear modes at the horizon by solv-

ing the second order equation for Ψ_0 . We illustrate this in Fig. 5 by plotting the amplitude of the second order Ψ_0 for the $\begin{pmatrix} 220+ \\ 220+ \end{pmatrix}$ QQNM, divided by the amplitudes of the linear modes at null infinity for normalization.

Additional detectability plots

In this section, we provide additional SNR plots for various QQNMs. Following the main text, we still consider two scenarios: For CE, we assume a binary system with a total mass of $100M_\odot$ and a luminosity distance of 410 Mpc. For LISA, we set $M_{\text{tot}} = 8 \times 10^6 M_\odot$ at a redshift of $z = 1$.

Figure 6 focuses on the QQNM $\begin{pmatrix} 2, 2, 0, + \\ 2, 2, 0, + \end{pmatrix}$, as studied in [42]. Unlike their Fig. 6, where the SNR peaks at $q \gtrsim 2$, our calculation shows that it decreases mono-

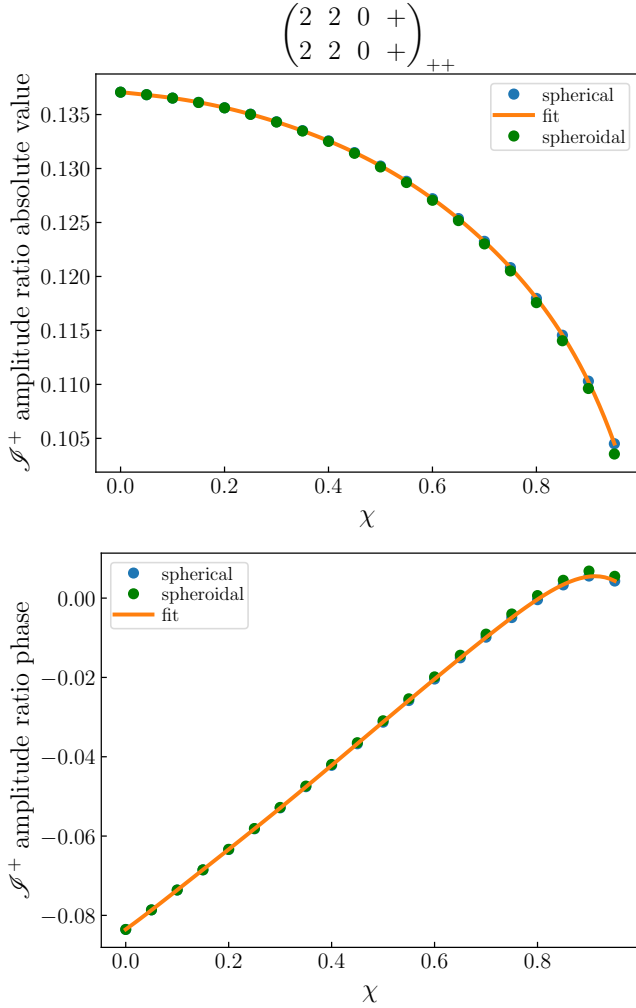


FIG. 3. Magnitude (top) and phase (bottom) of R_{++} for the QQNM $\begin{pmatrix} 220+ \\ 220+ \end{pmatrix}$ at null infinity, using spin-weighted spherical (blue dots) and spheroidal (green dots) harmonics

tonically with q . This quadratic mode is within the detectable range of both detectors.

Figure 7 considers $\begin{pmatrix} 4, 4, 0, + \\ 2, -2, 0, - \end{pmatrix}$. The SNR increases with χ_{eff} , and becomes the maximum at $q \sim 4.5$. While this mode might be weak for CE, it is still detectable with LISA.

Finally, to complement the discussion in the main text, we provide the detectability of $\begin{pmatrix} 3, 3, 0, + \\ 2, -2, 0, - \end{pmatrix}$ and $\begin{pmatrix} 3, 3, 0, + \\ 2, 2, 0, + \end{pmatrix}$ with LISA in Figs. 8 and 9, respectively. Figure 10 presents the SNR dependence of $\begin{pmatrix} 3, 3, 0, + \\ 2, -2, 0, - \end{pmatrix}$ on progenitor binaries' total mass M_{tot} , with $q = 2.75$, $\chi_{\text{eff}} = 0.9$. For CE, we choose $D_L = 410$ Mpc, while for LISA we set $z = 1$.

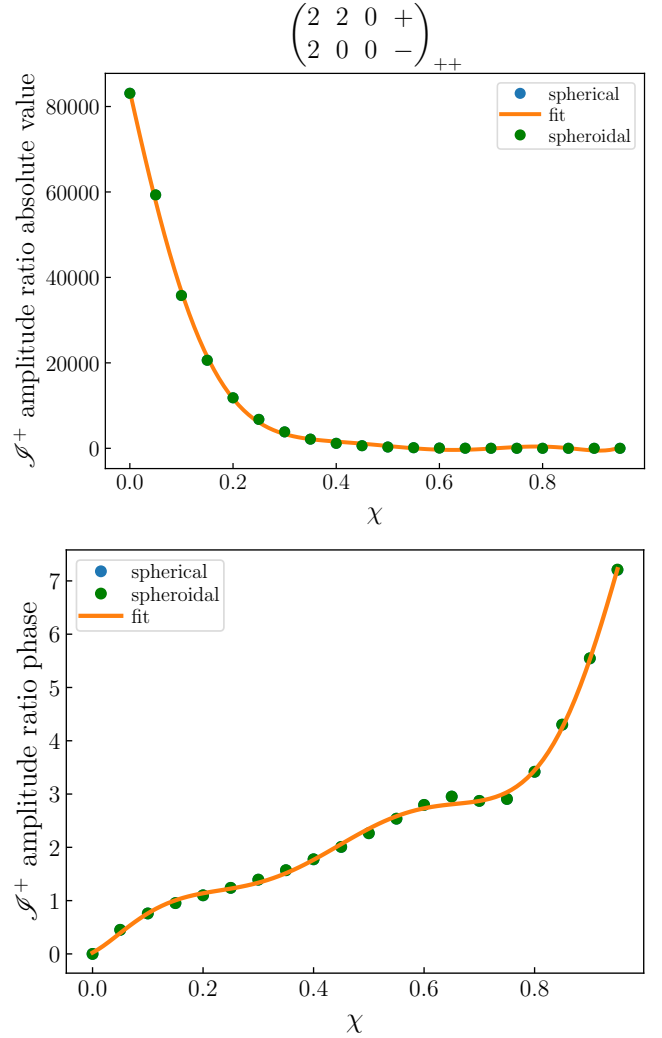


FIG. 4. Magnitude (top) and phase (bottom) of R_{++} for the QQNM $\begin{pmatrix} 220+ \\ 200- \end{pmatrix}$ at null infinity, using spin-weighted spherical (blue dots) and spheroidal (green dots) harmonics. The code becomes problematic as $\chi \rightarrow 0$, and R_{++} diverges.

Parity of linear and quadratic quasinormal modes

In this section we will discuss the relationship between the positive and negative frequency modes used in QNM analysis to even-parity (polar) and odd-parity (axial) modes. First, we note that the parity transformation $P_- : (\theta, \phi) \rightarrow (\pi - \theta, \phi + \pi)$ is a symmetry of the background Kerr spacetime. Furthermore, the QNM boundary conditions are also preserved by the parity operator, therefore QNMs are sent to QNMs.

Consider a linear mode $L = (\ell, m, n, p)$ with amplitude $\mathcal{A}_{\ell mn}^p$. The parity transformation P_- sends the waveform $h(\theta, \phi)$ to $\bar{h}(\pi - \theta, \phi + \pi)$ [56], the waveform

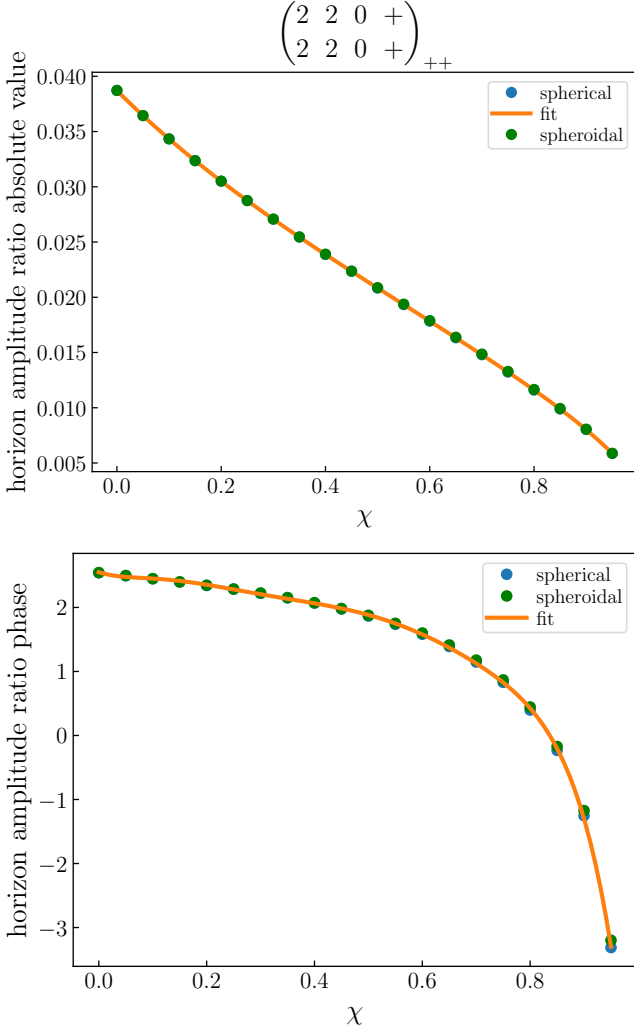


FIG. 5. Magnitude (top) and phase (bottom) of the amplitude ratio at the horizon for the QQNM $\begin{pmatrix} 220+ \\ 220+ \end{pmatrix}$, using spin-weighted spherical (blue dots) and spheroidal (green dots) harmonics

transforms as

$$\mathcal{A}_{\ell mn}^p e^{-i\omega_{\ell mn}^p u} {}_{-2}S_{\ell m}(\theta, \phi; a\omega_{\ell mn}^p) \quad (30)$$

$$\begin{aligned} &\rightarrow \bar{\mathcal{A}}_{\ell mn}^p e^{+i\bar{\omega}_{\ell mn}^p u} {}_{-2}\bar{S}_{\ell m}(\pi - \theta, \phi + \pi; a\bar{\omega}_{\ell mn}^p) \\ &= (-1)^{\ell+m} \bar{\mathcal{A}}_{\ell mn}^p e^{-i\bar{\omega}_{\ell, -m, n}^p u} {}_{-2}S_{\ell(-m)}(\theta, \phi; a\bar{\omega}_{\ell(-m)n}^p), \end{aligned} \quad (31)$$

where we have used Eq. (1) to rewrite the frequency, and the following properties of spin weighted spheroidal harmonics [57]:

$${}_s\bar{S}_{\ell m}(\theta, \phi; a\bar{\omega}) = (-1)^{s+m} {}_{-s}S_{\ell(-m)}(\theta, \phi; -a\bar{\omega}), \quad (32)$$

$${}_sS_{\ell m}(\pi - \theta, \phi + \pi; a\bar{\omega}) = (-1)^\ell {}_{-s}S_{\ell m}(\theta, \phi; a\bar{\omega}). \quad (33)$$

Therefore, the parity transformation takes the $L =$

(ℓ, m, n, p) mode with amplitude $\mathcal{A}_{\ell mn}^p$ to the mode $\bar{L} = (\ell, -m, n, -p)$ mode with amplitude $(-1)^{\ell+m} \bar{\mathcal{A}}_{\ell mn}^p$. We will refer to \bar{L} as the conjugate mode of L . Furthermore, by taking a linear combination of the linear modes L and its conjugate mode \bar{L} , we can construct solutions that are eigenvectors of the parity operator. In particular, the even parity sector is when the eigenvalue is $(-1)^{\ell+m}$, and the odd parity sector is when the eigenvalue is $(-1)^{\ell+m+1}$. The sign comes because the even and odd parity sectors are traditionally separated using the sign arising from the reversal of orientation rather than the parity operator P_- , giving rise to these signs.

Consequently, if we have the combination of $L = (\ell, m, n, p)$ and $\bar{L} = (\ell, -m, n, -p)$ modes with amplitudes $\mathcal{A}_{\ell mn}^p = \bar{\mathcal{A}}_{\ell(-m)n}^{-p}$, then combination of modes is even. If, on the other hand, $\mathcal{A}_{\ell mn}^p = -\bar{\mathcal{A}}_{\ell(-m)n}^{-p}$, the combination of modes is odd.

Consequently, an even or odd combination of pairs of linear modes L_1, \bar{L}_1 , and L_2, \bar{L}_2 gives rise to 4 quadratic modes that arise from their cross-terms: $(L_1; L_2)$, (L_1, \bar{L}_2) , $(\bar{L}_1; L_2)$ and $(\bar{L}_1; \bar{L}_2)$. Here each quadratic mode is contributed to by 3 channels. However, as we will see, not all 12 of the amplitude ratios are independent. The parity symmetry of the Kerr background will reduce it to 6 independent quadratic ratios.

Parity symmetry for quadratic amplitude ratios.— Let us now use the parity symmetry to relate amplitude ratios. Consider $Q = \begin{pmatrix} \ell_1 & m_1 & n_1 & p_1 \\ \ell_2 & m_2 & n_2 & p_2 \end{pmatrix}_{++}$, a quadratic mode with frequency ω_Q produced using the channel $(+, +)$. While the quadratic modes do not have spheroidal harmonic angular dependence anymore, the strain at infinity can be decomposed into spheroidal harmonics, so that the quadratic strain h from this mode is given by

$$h_Q = \sum_{\ell'} \mathcal{A}_1 \mathcal{A}_2 R_{++}^{Q, \ell'} {}_{-2}S_{\ell'(m_1+m_2)}(\theta, \phi; a\omega_Q) e^{-i\omega_Q u}. \quad (34)$$

Where $R_{++}^{Q, \ell'}$ is the amplitude ratio for the quadratic mode Q with child harmonics $(\ell', m_1 + m_2)$ with the $(+, +)$ channel, \mathcal{A}_1 is the amplitude of the mode (ℓ_1, m_1, n_1, p_1) and \mathcal{A}_2 is the amplitude of the mode (ℓ_2, m_2, n_2, p_2) . Under a parity transformation, the linear modes transform to $(\ell_1, -m_1, n_1, -p_1)$ and $(\ell_2, -m_2, n_2, -p_2)$ with amplitudes $(-1)^{\ell_1+m_1} \bar{\mathcal{A}}_1$ and $(-1)^{\ell_2+m_2} \bar{\mathcal{A}}_2$ respectively. Furthermore, under the parity transformation, the quadratic mode (34) transforms to the quadratic mode $\bar{Q} = \begin{pmatrix} \ell_1 & -m_1 & n_1 & -p_1 \\ \ell_2 & -m_2 & n_2 & -p_2 \end{pmatrix}_{++}$. We will refer to \bar{Q} as the conjugate mode of Q .

$$\begin{aligned} h_{\bar{Q}} &= \sum_{\ell'} (-1)^{\ell'+m_1+m_2} \\ &\quad \times \bar{R}_{++}^{Q, \ell'} \bar{\mathcal{A}}_1 \bar{\mathcal{A}}_2 e^{-i\omega_{\bar{Q}} u} {}_{-2}S_{\ell', -(m_1+m_2)}(\theta, \phi; a\omega_{\bar{Q}}). \end{aligned} \quad (35)$$

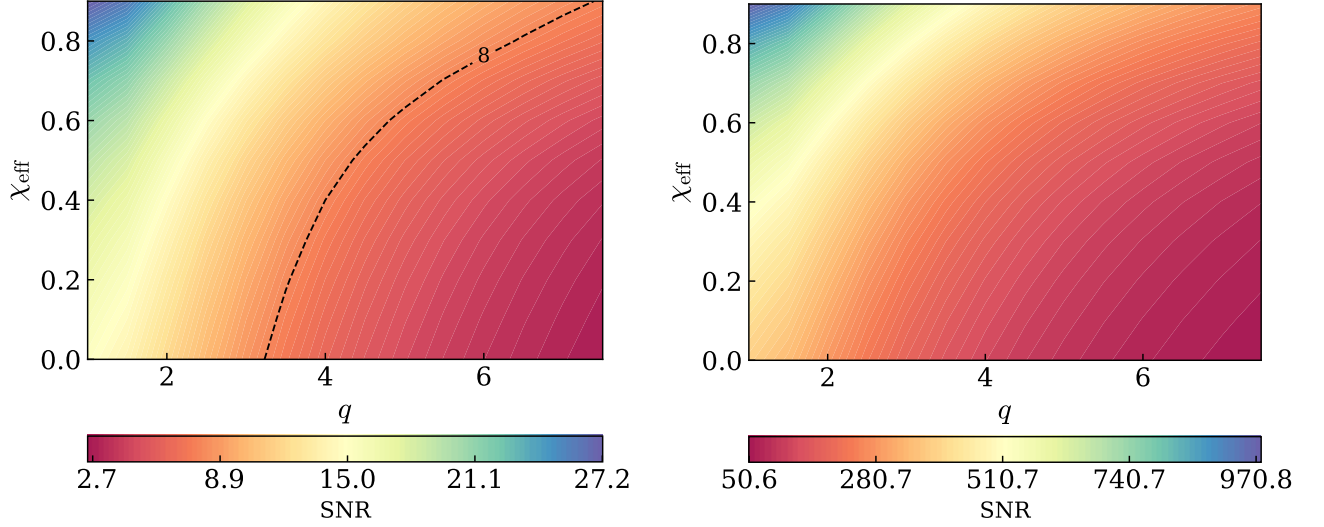


FIG. 6. The SNR of $\begin{pmatrix} 2, & 2, & 0, & + \\ 2, & 2, & 0, & + \end{pmatrix}$, assuming CE (left) and LISA (right).

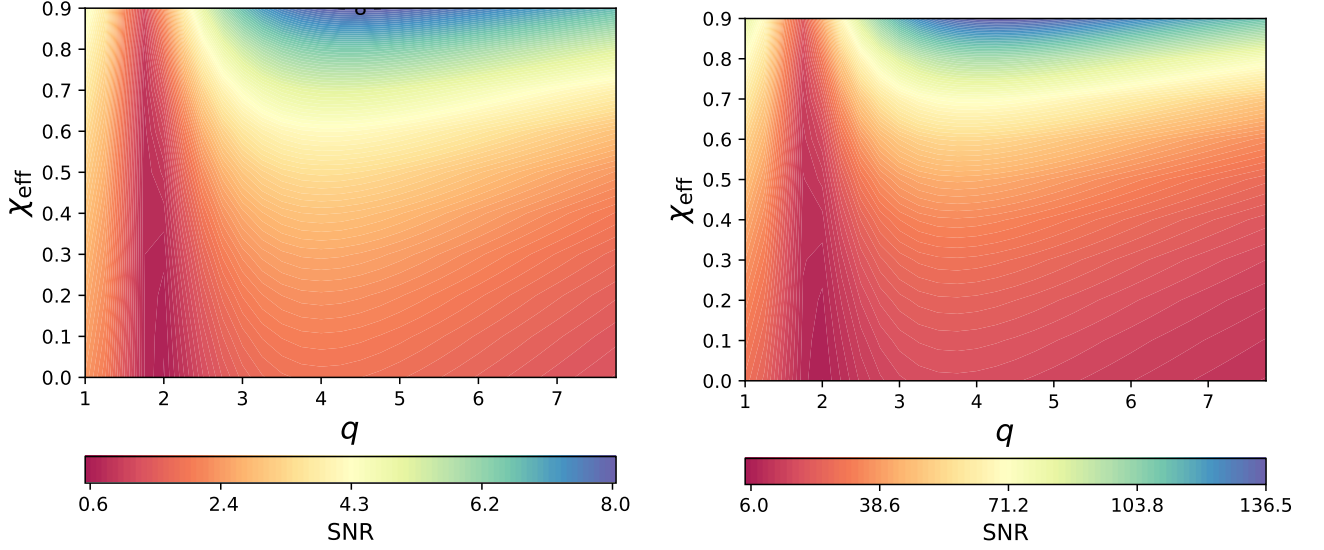


FIG. 7. The SNR of $\begin{pmatrix} 4, & 4, & 0, & + \\ 2, & -2, & 0, & - \end{pmatrix}$, assuming CE (left) and LISA (right).

Dividing the amplitude of this quadratic mode by the amplitudes of the linear modes gives us the coupling coefficient $R_{++}^{\bar{Q},\ell'}$ for the \bar{Q} mode, namely that

$$R_{++}^{\bar{Q},\ell'} = (-1)^{\ell'+\ell_1+\ell_2} \bar{R}_{++}^{\bar{Q},\ell'}. \quad (36)$$

Similarly, the above analysis applies to any channel

(c_1, c_2) , giving us

$$R_{c_1 c_2}^{\bar{Q},\ell'} = (-1)^{\ell'+\ell_1+\ell_2} \bar{R}_{c_1 c_2}^{\bar{Q},\ell'}. \quad (37)$$

Furthermore, note that while we used the spheroidal basis for this analysis, Eq. (36) is valid even for the amplitude ratio computed using the spin-weighted spherical harmonic basis. Thus, the amplitude ratio of a quadratic mode can be expressed in terms of the amplitude ratio of its conjugate mode.

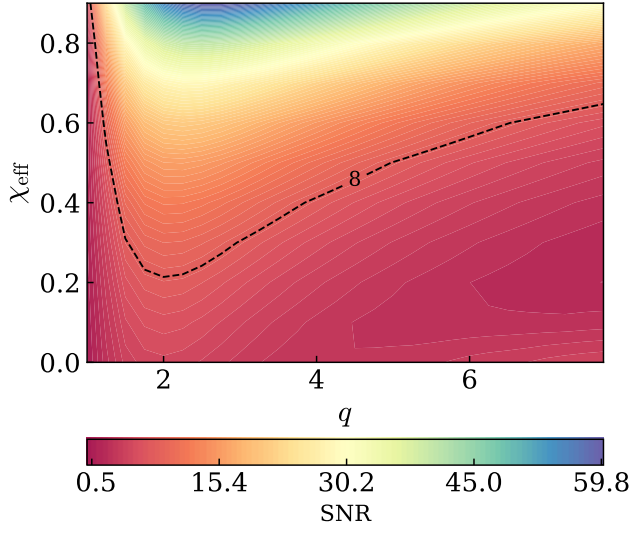


FIG. 8. The SNR of $\begin{pmatrix} 3, & 3, & 0, & + \\ 2, & -2, & 0, & - \end{pmatrix}$, assuming LISA.

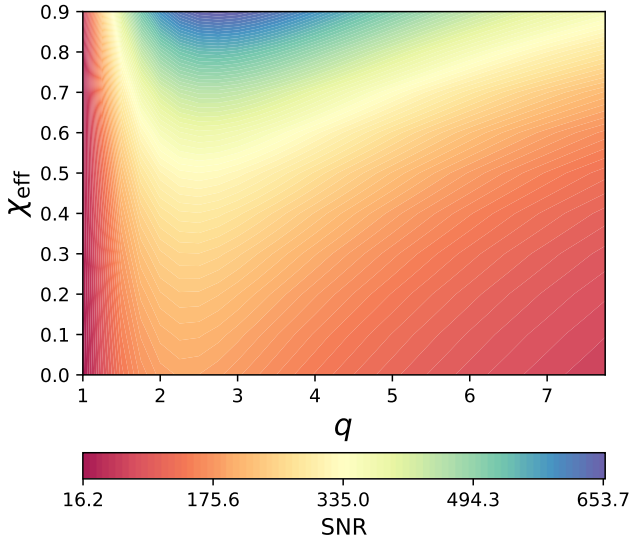


FIG. 9. The SNR of $\begin{pmatrix} 3, & 3, & 0, & + \\ 2, & 2, & 0, & + \end{pmatrix}$, assuming LISA.

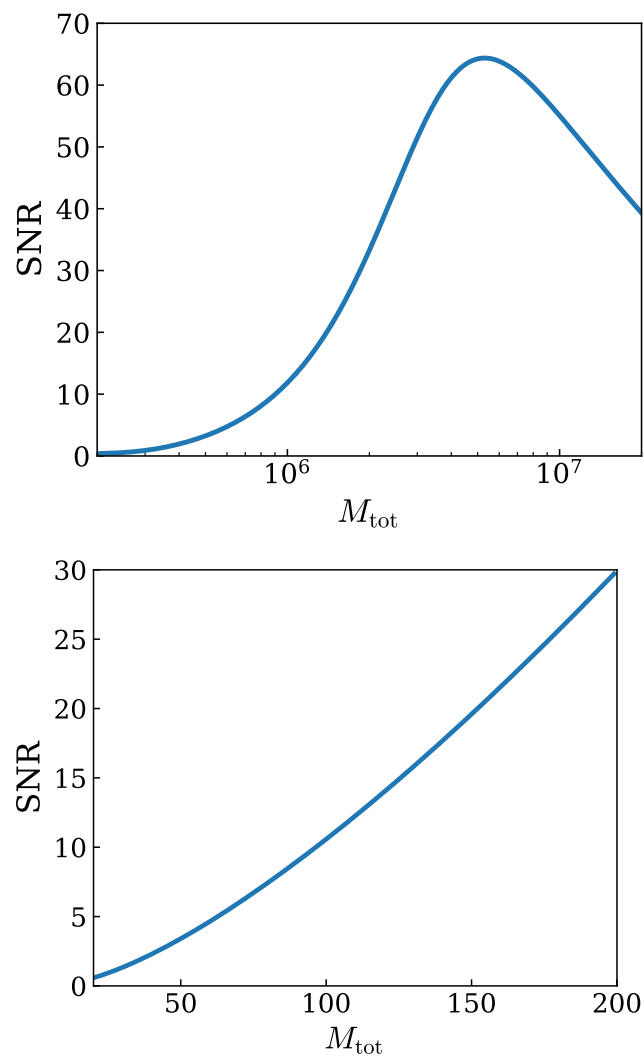


FIG. 10. The SNR dependence of $\begin{pmatrix} 3, & 3, & 0, & + \\ 2, & -2, & 0, & - \end{pmatrix}$ on progenitor binaries' total mass M_{tot} , using LISA (top) and CE (bottom), with $q = 2.75$, $\chi_{\text{eff}} = 0.9$. For CE, we choose $D_L = 410$ Mpc, while for LISA we set $z = 1$.